

# Deakin Research Online

*Deakin University's institutional research repository*

**This is the published version (version of record) of:**

Howlett, Patrick C., Efthimiadis, Jim, Hale, Penny, van Riessen, Grant A., MacFarlane, Douglas R. and Forsyth, Maria 2010, Characterization of the magnesium alloy AZ31 surface in the ionic liquid trihexyl(tetradecyl)phosphonium bis(trifluoromethanesulfonyl)amide, *Journal of the electrochemical society*, vol. 157, no. 11, pp. C392-C398.

**Available from Deakin Research Online:**

<http://hdl.handle.net/10536/DRO/DU:30035813>

**Reproduced with kind permission of the copyright owner.**

**Copyright :** ©2010, The Electrochemical Society



## Characterization of the Magnesium Alloy AZ31 Surface in the Ionic Liquid Trihexyl(tetradecyl)phosphonium Bis(trifluoromethanesulfonyl)amide

Patrick C. Howlett,<sup>a,\*</sup> Jim Efthimiadis,<sup>a</sup> Penny Hale,<sup>b</sup> Grant A. van Riessen,<sup>b</sup> Douglas R. MacFarlane,<sup>c</sup> and Maria Forsyth<sup>a,\*</sup>

<sup>a</sup>Department of Materials Engineering and <sup>c</sup>School of Chemistry, ARC Centre of Excellence for Electromaterials Science, Monash University, Victoria 3800, Australia

<sup>b</sup>Centre for Materials and Surface Science, Department of Physics, School of Engineering and Mathematical Sciences, Faculty of Science, Technology and Engineering, La Trobe University, Victoria 3056, Australia

Commercially available magnesium alloy AZ31 is extensively used in structural engineering components although, like many magnesium-based materials, it suffers from poor corrosion resistance, particularly in marine environments, which limit wider application. Previously, the ionic liquid (IL) trihexyl(tetradecyl)phosphonium bis(trifluoromethanesulfonyl)amide ( $[P_{66614}][NTf_2]$ ) was shown to improve the corrosion resistance of magnesium alloy AZ31 in humid environments and in the presence of chloride-containing aqueous environments. Here, we investigate the morphology and composition of the protective surface film that forms upon immersion of the Mg alloy in the IL, using grazing angle X-ray diffraction (XRD), X-ray photoelectron spectroscopy (XPS), time of flight-secondary-ion mass spectrometry (TOF-SIMS), solid-state NMR, and transmission electron microscopy (TEM). XRD indicates that an amorphous film is present on the surface subsequent to exposure to the  $[P_{66614}][NTf_2]$  IL, whereas XPS etching experiments indicate that the film is multilayered. The innermost layer is predominantly inorganic fluoride salts as well as native oxide/hydroxide surface species. TOF-SIMS spectra support these observations and indicate an outermost, thin, adherent layer of IL species. Multinuclear NMR spectroscopy confirms the presence of a multiphase composition as well as the presence of metal fluorides and complex organic species. The surface film appears to be of the order of 100 nm according to the TEM/energy-dispersive X-ray spectroscopy observations.

© 2010 The Electrochemical Society. [DOI: 10.1149/1.3486119] All rights reserved.

Manuscript submitted June 1, 2010; revised manuscript received August 9, 2010. Published September 23, 2010.

In recent times, magnesium alloys have been increasingly employed as lightweight structural engineering components, particularly in the automotive and aeronautic transport industries (e.g., as cast engine and transmission housings).<sup>1</sup> These applications are attributed to the good processability,<sup>2</sup> high specific strength and stiffness,<sup>3</sup> and low density of magnesium,<sup>4</sup> leading to weight reduction and thus significant cost-effective benefits in energy consumption and fuel economy.<sup>5</sup> To meet the stringent environmental requirements being set for automobile manufacturing, energy efficiency, and CO<sub>2</sub> emission reduction, magnesium use is expected to further increase at a rapid rate.<sup>3</sup> Furthermore, magnesium is the eighth most terrestrially abundant element (~2% abundance of the earth's crust)<sup>6</sup> and is cheap to extract. However, magnesium's poor corrosion properties are limiting, particularly in commercial and industrial applications.<sup>7</sup> To date, a definitive understanding of magnesium's long-term service, residual life, treatment efficacy, failure mechanistic behavior, and corrosion protection capacity is at a relatively early stage of development.<sup>8</sup> Magnesium maintains a passive, atmospheric-formed surface film comprising a magnesium oxide/hydroxide and carbonate film a few nanometers in thickness<sup>9</sup> that may limit coating uniformity and adhesion.<sup>10</sup> The film is susceptible to attack,<sup>7</sup> particularly when exposed to moist environments with increasing relative humidity<sup>8</sup> and temperature.<sup>9</sup> The oxide film is poorly protective but may provide useful adhesion to secondary protective surface coatings, although the characterization and nature of the metallic and/or oxide magnesium film in combination with such surface films remain limited.<sup>11,12</sup> A wide variety of chemical surface treatments,<sup>13</sup> protective films, and coatings have been developed and utilized to modify magnesium's corrosion performance and provide a barrier between metal and environment.<sup>14</sup> These treatments range from electrolytic,<sup>15</sup> anodization,<sup>16</sup> electroplating, ion implantation,<sup>17</sup> conversion-coating<sup>18</sup> chromate-based primers and solutions (with subsequent organic top coat),<sup>1</sup> phosphate-permanganate,<sup>10</sup> and vapor-phase processes. Less toxic alternatives have been sought

such as calcium phosphate surface coatings for example, which have shown promising application as bioabsorbable/bioactive biomaterials.<sup>21</sup>

The corrosion characteristics of magnesium and its alloys are dependent on the alloy chemistry and the exposed environmental conditions.<sup>22</sup> Furthermore, the complex microstructural possibilities for these alloys can lead to nonuniformities in the surface film, thereby making it ineffective in terms of corrosion protection.<sup>23,24</sup> AZ31 is an aluminum containing magnesium alloy<sup>9</sup> of roughly 3% Al, 1% Zn, (with minor, ~0.3% Mn additions) and many attempts have been made to improve the corrosion characteristics of this alloy.<sup>12</sup> This alloy is the focus of our discussion where a novel ionic liquid (IL) chemical treatment is used to form a protective surface film.

ILs (i.e., salts that melt below 100°C) are capable of providing a protective coating against corrosion for Mg alloys.<sup>7,23-29</sup> ILs are organic salts, comprising an organic cation and either an inorganic or organic anion that are liquid below 100°C. ILs are generally non-volatile, with a high thermal stability and a wide and stable electrochemical window,<sup>30</sup> nonflammable, can have a low toxicity, and thus show promise as replacements for toxic molecular solvents.<sup>31</sup> The large number of cation-anion combinations, coupled with the wide range of desirable properties, has given ILs the title "designer solvents."<sup>32</sup> Tetradecyl(trihexyl)phosphonium ( $[P_{66614}]^+$ ) is a large, hydrophobic cation that has been used to synthesize many ILs<sup>25,33</sup> with a wide range of anions, whose properties, including viscosity, conductivity, thermal properties, and corrosion characteristics on ZE41<sup>26,34</sup> and AZ31<sup>25,27</sup> magnesium alloys, have been studied.

Recently, we have investigated an IL based on the  $[P_{66614}]^+$  cation and the bis(trifluoromethanesulfonyl)amide ( $[NTf_2]^-$ ) anion for its use in the protection of the AZ31 magnesium alloy (Fig. 1).<sup>29,35,36</sup> Indeed, the  $[P_{66614}][NTf_2]$  IL produces an order of magnitude reduction in the corrosion rate on pure Mg and AZ31. The presence of a passivating film as indicated by impedance spectroscopy and scanning electron microscopy observations depends on the immersion time and temperature.

In this work, we further investigate the morphology and composition of the surface film formed on the AZ31 magnesium alloy in

\* Electrochemical Society Active Member.

<sup>z</sup> E-mail: patrick.howlett@eng.monash.edu.au; maria.forsyth@eng.monash.edu.au

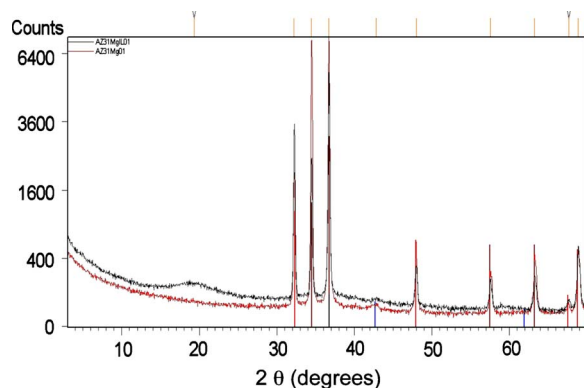


**Figure 1.** (Color online) Grazing angle XRD patterns for the AZ31 Mg alloy (lower: Red) and that of the AZ31 Mg alloy exposed to the IL (upper: Black). Sharp lines indicate the phases for Mg and MgO, which dominate the patterns.

the  $[P_{66614}][NTf_2]$  IL using many surface-sensitive techniques including grazing angle X-ray diffraction (XRD), X-ray photoemission spectroscopy (XPS), time of flight–secondary-ion mass spectrometry (TOF-SIMS) mapping, NMR, and electron microscopy. We develop an understanding of the reactivity of the interfacial region among the magnesium alloy, the native oxide film, and the IL to ultimately understand the factors that can lead to improvement in the corrosion resistance of this alloy.

### Experimental

**Material preparation.**— An AZ31 magnesium alloy was polished with SiC paper, progressively down to grit 4000, and further polished with  $0.05\ \mu\text{m}$   $\text{Al}_2\text{O}_3$  paste. After polishing, samples were rinsed thoroughly with distilled water and ethanol and dried with nitrogen gas. The samples were treated at room temperature by immersion in the IL  $[P_{66614}][NTf_2]$  for either 15 or 20 h. For this work, these treatment times were viewed as producing an equivalent film. Following immersion, the samples were subsequently cleaned with distilled water, ethanol, and again with distilled water. The samples were then dried with nitrogen gas and stored in a desiccating chamber for subsequent characterization.

**Transmission electron microscopy imaging.**— Transmission electron microscopy (TEM) imaging was used to visualize the IL coating on the surface of the AZ31 magnesium alloy to clarify the nature and origin of any observable surface features. Sample preparation for TEM involved the coating of AZ31 with IL  $[P_{66614}][NTf_2]$  for 65 h with storage within a vacuum desiccator. The longer immersion time was selected in an attempt to yield a thicker, more discernible surface film. An IL-coated AZ31 alloy was prepared by shaping the alloy, originally to a pyramid, in an effort to minimize microtome trimming and surface film disruption. A DU3530 Diatome 3.0 mm ( $35^\circ$  included angle) ultramicrotomy knife, using a Reichert-Jung Ultracut E Ultramicrotome, was used to produce sectioned TEM specimens of  $\sim 40\ \text{nm}$  thickness at ambient temperature. The microtomed samples were subsequently floated on deionized water to minimize alloy degradation and were loaded onto hexagonal copper (Cu) TEM grids containing a lacey carbon film. Multiple metallographic sections were prepared in the thickness range 40–100 nm. The ideal thickness for this alloy was determined to be  $\sim 100\ \text{nm}$ . Multiple sectioned samples were imaged and analyzed using a JEOL2010 transmission electron microscope equipped with an SIS MegaView 3 charge-coupled device camera and a Thomson Scientific WinEDS energy-dispersive X-ray spectroscopy (EDXS) system. The transmission electron microscope was operated at an accelerating voltage of 100 kV to avoid specimen damage. Higher voltages resulted in visible specimen damage to both the IL coating and the alloy substrate. Images were recorded at various

magnifications up to  $1,000,000\times$ , although a typical operating magnification was  $200,000\times$ . Elemental analysis (EDXS recorded between 0 and 10 keV) was performed on the sample surfaces to establish the elemental distribution present using a spot size of 25 nm.

**Grazing angle XRD.**— XRD experiments were conducted using a PANalytical Multipurpose diffractometer in a parallel beam configuration (grazing angle). The incident beam consisted of a Cu tube, a Cu X-ray mirror,  $0.5^\circ$  divergence slit, 0.04 rad Soller slits, and a 4 mm mask. The diffracted beam consisted of a  $0.09^\circ$  parallel plate collimator, 0.04 rad Soller slits, a Cu detector slit, a flat graphite monochromator, and a mini proportional detector. Data were collected from  $3$  to  $70^\circ$   $2\theta$ , a step size of  $0.02^\circ$  per step for 5 s per step. The angle of the incident beam was  $1^\circ$ . Samples of  $\sim 1\ \text{cm}^2$  blocks were used in the measurements.

**NMR.**— Solid-state NMR spectroscopy was performed using a Bruker ASX300 solid-state spectrometer, using a 7.05 Tesla magnetic wide bore with two channels,  $^1\text{H}$  and  $^{19}\text{F}$  species investigated at 300.1 and 235.3 MHz, respectively. Magic angle spinning (MAS) was conducted using a Bruker 4 mm MAS probe at a rate of  $\sim 10\ \text{kHz}$ . Sample preparation for NMR measurements involved removal of the surface film from the AZ31 surface, which was immersed for 6 days in the IL ( $[P_{66614}][NTf_2]$ ). The removed material was subsequently mixed with titania ( $\text{TiO}_2$ ) to disperse it homogeneously within the ceramic NMR rotor.  $^{19}\text{F}$  (235.3 MHz,  $\text{CFCl}_3$  reference, 5 s recycle delay) and  $^{31}\text{P}$  (121.4 MHz,  $\text{H}_3\text{PO}_4$  reference, 3 s recycle delay) were measured for each sample. Before commencing the initial experiments, the sample was stored in the rotor for 24 h.

**TOF-SIMS.**— The TOF-SIMS analyses were performed with a PHI TRIFT II (model 2100) spectrometer (PHI Electronics Ltd.) equipped with a  $^{69}\text{Ga}$  liquid metal ion gun. A 25 keV pulsed (repetition rate of  $\sim 10\ \text{kHz}$ ) primary ion beam was used. For charge compensation, samples were flooded with low energy electrons ( $\sim 20\ \text{eV}$ ) between each primary ion pulse. Mass axis calibration was done with  $\text{CH}_3^+$ ,  $\text{C}_2\text{H}_5^+$ , and  $\text{C}_3\text{H}_7^+$  in the positive mode and with  $\text{CH}^-$ ,  $\text{C}_2\text{H}^-$ , and  $\text{Cl}^-$  in the negative mode of operation. In this study, typical analysis time ranged from 2 to 5 min with primary ion doses of around  $3 \times 10^{12}$  ions per  $\text{cm}^2$ . The mass resolution was typically greater than 7500 at  $m/z = 29$ . Multielemental spectra were acquired in both the positive and negative SIMS statuses and depth profiling was performed. A  $100 \times 100\ \mu\text{m}$  area was sputtered at 5 s intervals and analysis was performed on a  $50 \times 50\ \mu\text{m}$  area for 5 s for a 50 min period using 0.5 keV  $\text{Cs}^+$  ions with an energy of 0.5 kV.

**XPS.**— The sample was mounted on an XPS sample stud using a conductive carbon adhesive tape. Spectra were acquired on a Kratos Axis Ultra imaging XPS spectrometer (Kratos, U.K.). An aluminum monochromated X-ray source operating at 10 mA and 15 kV (150 W) was used. The hybrid analysis mode was used, which provided a sampling area of  $300 \times 700\ \mu\text{m}$ . Survey spectra were acquired at 160 eV pass energy and high resolution region spectra were acquired at 20 eV pass energy. For depth profiling, the surface was sputtered using an argon ion gun operating at 15 mA and 5 kV. Instrument operation and peak fitting were performed using the XPS Axis Ultra software. A 70:30 Gaussian:Lorentzian algorithm was used to fit the peaks to obtain quantitative results. The fit produced an estimated  $\pm 10\%$  error in the atomic concentration determined for each peak.

### Results and Discussion

The grazing angle XRD pattern taken at an incidence angle of  $1^\circ$  is shown for both the polished AZ31 specimen and the alloy immersed in phosphonium IL. The broad peak centered  $\sim 19^\circ$  is indicative of an amorphous phase on the surface; however, all sharp reflections are related to the underlying alloy surface that consists of Mg and a MgO layer.

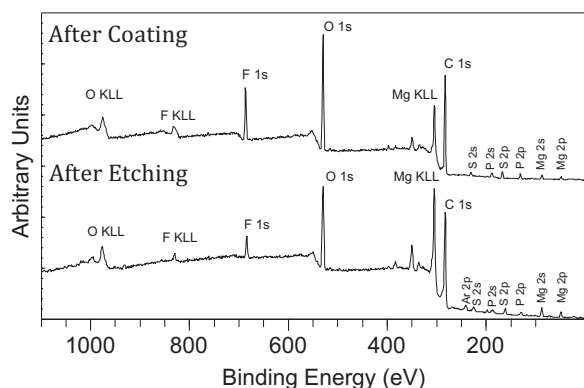


**Figure 2.** XPS survey spectra acquired for a 15 h  $[P_{66614}][NTf_2]$  treated AZ31 sample (after coating) and after 10 min argon ion etching (after etching).

The chemical composition of the IL film, both on the “as-prepared” IL treated surface and through the depth of the film, has been investigated by XPS and TOF-SIMS. Figure 2 gives the XPS survey spectra for the AZ31 IL treated surface before and after 10 min of argon ion beam etching. Figure 3 shows higher resolution

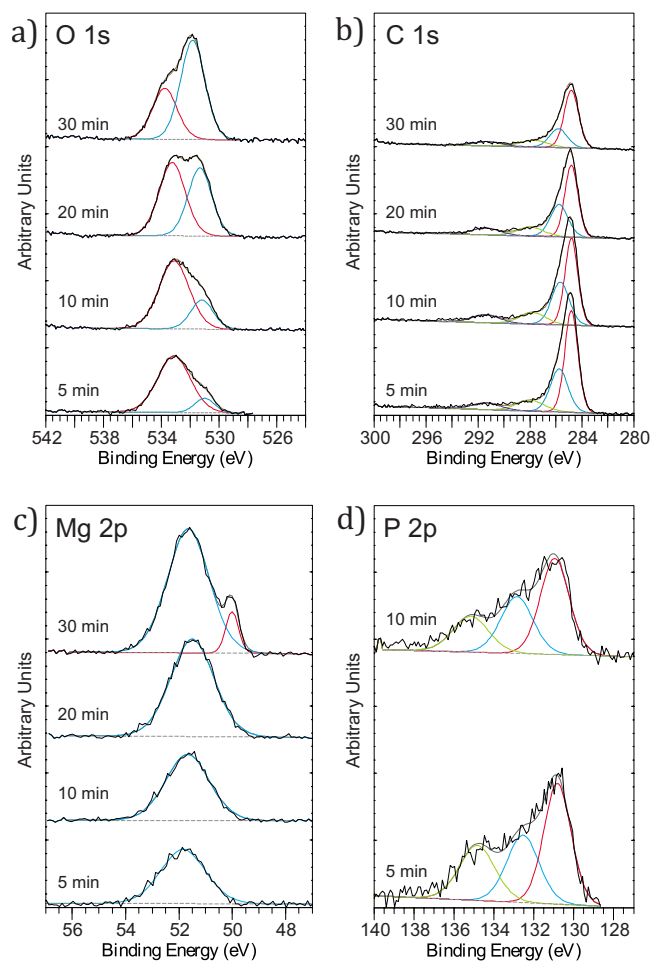


**Figure 3.** (Color online) XPS region spectra acquired for a 15 h  $[P_{66614}][NTf_2]$  treated AZ31 sample at successive etching intervals for (a) O 1s, (b) C 1s, (c) Mg 2p, and (d) P 2p photoelectron lines. Peak heights are normalized to the most intense scan (i.e., O 1s = 6039 counts per second (CPS), C 1s = 4162 CPS, Mg 2p = 860 CPS, and P 2p = 192 CPS).

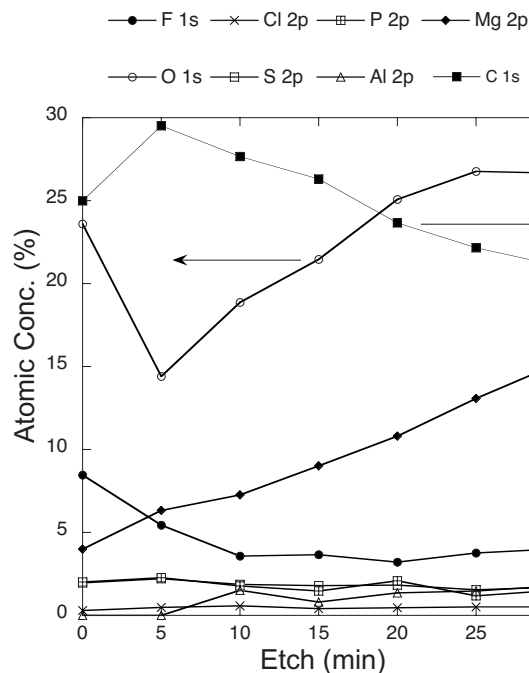


**Figure 4.** Graphical summary of the XPS survey spectra quantification acquired at 5 min intervals for each of the detected surface species. C 1s species dominate and are represented on the right y-axis for clarity.

spectra for the key C, O, P, and Mg elements as a function of etch time, whereas Fig. 4 summarizes the relative atomic concentration of the individual species through the film (i.e., as the surface is etched). The chemical state assignment of components fitted to the high resolution spectra acquired after various etch times is summarized in Table I.

The data here already provide a picture of the film morphology with the presence of both anion and cation moieties of the IL suggested to be present in the amorphous surface film. Notwithstanding the adventitious surface carbon contamination usually observed by XPS for samples exposed to air, the concentration of C is very large here and appears to be predominantly aliphatic C–C bonds on the nonetched surface. This would be expected if the cation was present in the film as each phosphonium cation has 32 alkyl carbons present. After etching, other species with higher binding energy (BE) increase in relative intensity, which could be indicative of anion and/or anion breakdown products containing C–F for example. This has also been suggested previously for a reactive lithium metal surface exposed to a  $[NTf_2]^-$ -based IL.<sup>37</sup>

The oxygen content decreases in the initial etch and then gradually increases again. The F species decrease by almost a factor of 2 after 10 min of etching and then stabilize at ~4% atomic concentration, and the other species attributed to the IL, namely P and S, are constant across all the etching times. The  $[NTf_2]^-$  anion contains six oxygen atoms per anion and, therefore, if it were adsorbed relatively intact on the surface, there would be a higher O content before etching. Subsequent O species are primarily attributed to the metal oxide and hydroxides (MgO/MgOH) and these would be expected to increase as the IL-based film is gradually removed. The increase in Mg and Al indicate that more of the underlying metal alloy substrate is observed as the amorphous surface film is etched away. Initially, the Mg species are predominantly Mg–O moieties; however, metal Mg (and Al) is eventually evident after 30 min of etching. The persistence of the S and P species in the XPS spectra suggests that either these elements are indeed present in the film as deposited or alternatively the etching process produces changes in the sample surface (e.g., by smearing, preferential sputtering, sample reduction, or X-ray degradation) that do not reflect its true composition. In

**Table I. XPS peak assignments for the 15 h [P<sub>6614</sub>][NTf<sub>2</sub>]<sup>-</sup> treated AZ31 alloy surface and etching profiling as a function of time for the elements C, O, F, P, Mg, and Al.**

| Photoelectron line and assignment | Atomic concentration % initial <sup>a</sup> (BE eV) | Atomic concentration % 5 min etch (BE eV) | Atomic concentration % 10 min etch (BE eV) | Atomic concentration % 20 min etch (BE eV) | Atomic concentration % 30 min etch (BE eV) |
|-----------------------------------|---|---|--|--|--|
| C 1s (C–C)                        | 58.3 <sup>a</sup> (283.0)                           | 32.4(285.0)                               | 28.2(285.0)                                | 23.5(285.0)                                | 26.0(285.0)                                |
| C 1s(C–O)                         |   | 18.5(286.1)                               | 19.1(286.0)                                | 14.4(286.3)                                | 10.4(286.1)                                |
| C1s (C=O)                         |   | 7.2(287.7)                                | 7.7(287.7)                                 | 5.9(288.4)                                 | 5.7(287.9)                                 |
| C 1s (C–F)                        |   | 4.5(291.5)                                | 5.6(291.5)                                 | 4.8(291.6)                                 | 3.7(291.7)                                 |
| O 1s (C–O)                        | 23.6 <sup>a</sup> (530.0)                           | 13.1(533.5)                               | 14.1(533.3)                                | 13.8(533.4)                                | 11.0(533.9)                                |
| O 1s (MgO/MgOH)                   |   | 5.0(531.5)                                | 7.4(531.5)                                 | 13.0(531.5)                                | 19.0(532.0)                                |
| F 1s (AlF <sub>3</sub> or C–F)    | 8.6 <sup>a</sup> (687.0)                            | 5.1(686.9)                                | 3.3(686.9)                                 | 2.8(686.9)                                 | 3.0(687.0)                                 |
| P 2p (alkyl phosphate)            | 2.0 <sup>a</sup> (131.0)                            | 1.2(130.9)                                | 0.9(130.9)                                 | 2.1 <sup>a</sup> (130.0)                   | 1.5 <sup>a</sup> (130.0)                   |
| P 2p (alkyl phosphate)            |   | 1.0(132.5)                                | 0.6(132.7)                                 |  |  |
| P 2p (P–F?)                       |   | 0.8(134.9)                                | 0.5(134.9)                                 |  |  |
| S 2p (P–S?)                       | 2.0 <sup>a</sup> (167.0)                            | 2.2(163.9)                                | 1.9(163.7)                                 | 1.8 <sup>a</sup> (161.0)                   | 1.7 <sup>a</sup> (162.0)                   |
| S 2p (MgS?)                       |   | 0.3(162.0)                                | 0.1(162.3)                                 |  |  |
| Al 2p (AlF <sub>3</sub> ?)        |   |   | 1.1(75.4)                                  | 1.4 <sup>a</sup> (72.0)                    | 2.0(75.7)                                  |
| Al 2p (Al <sup>o</sup> )          |   |   |  |  | 0.9(73.1)                                  |
| Mg 2p (MgO/MgF <sub>2</sub> )     | 4.0 <sup>a</sup> (48.0)                             | 8.2(52.0)                                 | 8.6(51.8)                                  | 12.7(51.6)                                 | 16.0(51.9)                                 |
| Mg 2p (Mg <sup>o</sup> )          |   |   |  |  | 2.3(50.2)                                  |

<sup>a</sup> Data from survey scan acquisition mode.

addition, the uncertainty in the determined relative atomic concentration for S and P is large because they present small peaks on a large background with significant noise. Thus, the XPS etching based conclusions must be tentative and ideally supported by other techniques, as we have used here. Notwithstanding these problems, the change in sample composition revealed provides useful insight into the compositional changes that occur throughout the thickness of the film.

In an earlier preliminary work,<sup>28</sup> TOF-SIMS analysis of the AZ31 alloy surface after being immersed for 20 h indicated a peak in the negative spectrum at  $m/z = 280$  (which represents the mass of the [NTf<sub>2</sub>]<sup>-</sup> anion) and the presence in the positive TOF-SIMS spectrum of a peak at  $m/z = 483$ , which provided clear evidence for the presence of the intact phosphonium cation. These data clearly indicated that both the anion and the cation were present on the topmost surface of the treated AZ31 alloy despite thorough washing of this surface before analysis. This complements the XPS data detailed above, which are not able to clearly identify intact anion on the surface. In view of TOF-SIMS being a more surface-sensitive technique, this also suggests a very thin outer anion/IL containing layer, most likely several monolayers thick, representing only a small fraction of the XPS sampling volume, which at 1486 eV is likely to be tens of nanometers deep. After a 10 min etch, the spectra changed considerably to show that these intact ions were no longer present on the surface. Furthermore, analysis of the secondary ion yields as a function of etch time suggested that the relative concentration of F<sup>-</sup> was greatest at the surface and decreased steadily with a concomitant increase in the relative concentration of O<sup>-</sup> and Mg-containing species with increasing etch time. Acquired spectra and etching data are presented in detail in Ref. 28 and Fig. 5 presents secondary ion maps obtained from the same data set. They clearly show that the F<sup>-</sup> distribution is essentially uniform before etching. After etching, the F<sup>-</sup> distribution is patchy and has been removed from a large fraction of the area. The O<sup>2-</sup> and OH<sup>-</sup> distributions (which are similar) show anticorrelation with the F<sup>-</sup> distribution (e.g., feature in the top left corner of each etched surface). Overall, the relative intensity of the species increases from left to right for

the (a) “after coating” and the reverse for the (b) after etching. Again, this is similar to the observations made for a reactive Li metal surface following a reaction with a NTf<sub>2</sub><sup>-</sup>-based IL using XPS.<sup>37</sup>

The presence of metal fluorides is also suggested by the <sup>19</sup>F solid-state NMR spectrum shown in Fig. 6 (the pure IL is shown for comparison in the inset). Although some intact [NTf<sub>2</sub>]<sup>-</sup> is expected from the TOF-SIMS spectra discussed above, the NMR certainly shows that a large fraction of the signal is due to additional species in the region 116–130 ppm, which may be attributed to either disordered metal fluoride (given that XRD showed that the surface was amorphous, this is indeed consistent) or alternatively CF<sub>2</sub> species, which may also result from breakdown products as previously suggested.<sup>23</sup> Even the peak nominally assigned to the [NTf<sub>2</sub>]<sup>-</sup> spe-

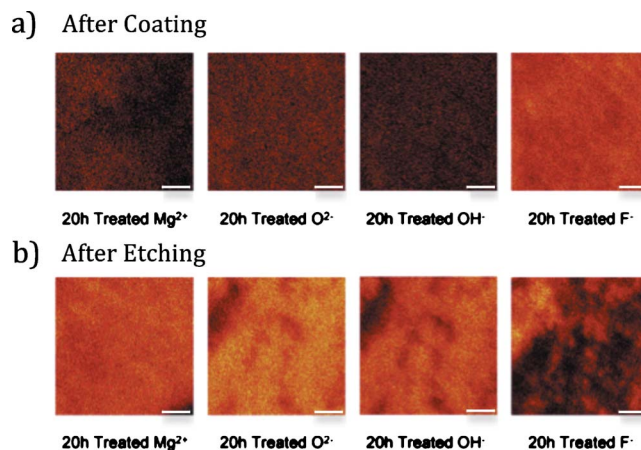


**Figure 5.** (Color online) TOF-SIMS maps (Mg<sup>2+</sup>, O<sup>2-</sup>, OH<sup>-</sup>, and F<sup>-</sup>) acquired from a 20 h [P<sub>6614</sub>][NTf<sub>2</sub>]<sup>-</sup> treated AZ31 sample (a) before and (b) after gallium ion etching. Scale bar = 10 μm.

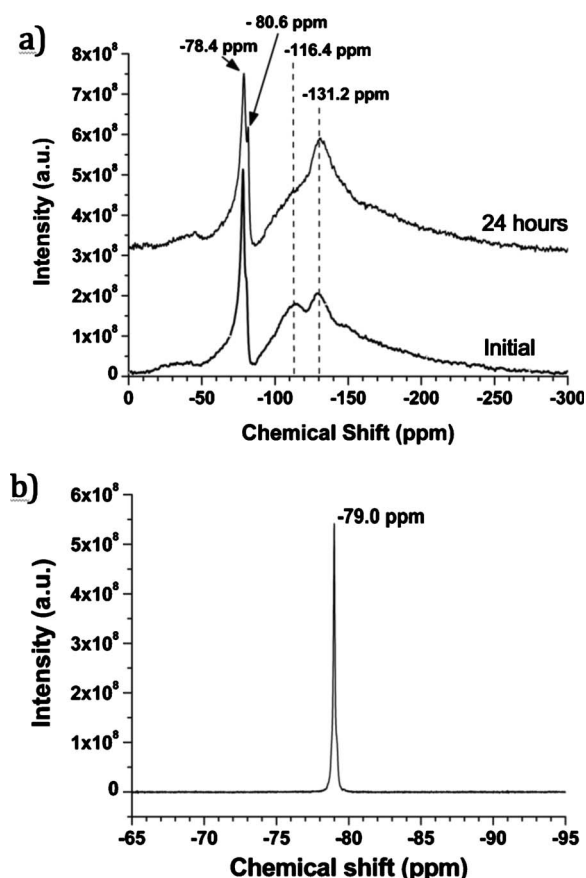


**Figure 6.** (a)  $^{19}\text{F}$  MAS solid-state NMR spectra for the 20 h  $[\text{P}_{66614}][\text{NTf}_2]$  treated AZ31 alloy surface, showing spectrum acquired initially after loading the rotor (lower) and after 24 h storage (upper). (b) The  $^{19}\text{F}$  spectrum for  $[\text{P}_{66614}][\text{NTf}_2]$  is shown for comparison.

cies shows some asymmetry and has shifted slightly from the pure IL resonance, which may be interpreted as some interaction between the  $[\text{NTf}_2]^-$  anion within the surface film. This is in contrast to the XPS data, which indicate a lower proportion of intact  $[\text{NTf}_2]^-$ , providing further support for the notion of a very thin layer of IL on the surface. NMR provides an analysis of the entire film and is thus sensitive to all of the anion/IL present on the surface. Another interesting observation from these NMR experiments is that the spectra were time-dependent, with significant changes occurring from the first spectrum collection immediately after loading the rotor and a day later ( $^{19}\text{F}$  spectra collected up to a week later showed less significant changes). The most pronounced change is in the growth of the resonance centered around  $-130$  ppm, which suggests that the reaction tending toward the metal fluoride still continues even after the surface has been removed from the AZ31 alloy. This could be in part due to the exposure of a fresh metal surface as a result of “grinding” the surface film from the alloy surface. This would continue to react in the rotor with any residual IL or indeed any breakdown products.

The  $^{31}\text{P}$  NMR spectrum (Fig. 7) shows only a very weak signal at 33 ppm, which is exactly related to phosphorus in the  $[\text{P}_{66614}]^+$  cation. There are no additional resonances and so, apparently, the cation’s presence is restricted to the outermost layers (as suggested by TOF-SIMS)<sup>28</sup> as an adsorption layer and no additional reaction with the alloy is observed.

In an attempt to provide a definitive detection of morphology and composition of the thin surface films produced on the alloy surface, TEM analysis of a microtomed section was undertaken. Samples were prepared with a prismatic geometry so that the section would,

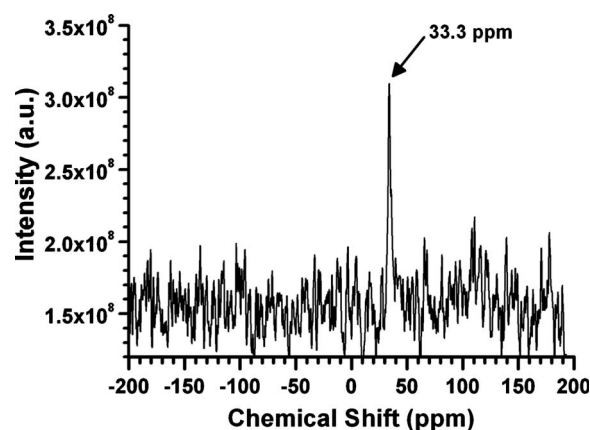


**Figure 7.**  $^{31}\text{P}$  MAS solid-state NMR spectrum for the 20 h  $[\text{P}_{66614}][\text{NTf}_2]$  treated AZ31 alloy surface.

in principal, show a well-defined ring of surface film around an otherwise metallic section. Figure 8 presents a TEM image of a sectioned AZ31 Mg alloy immersed in the IL for 65 h (this extended time was used to maximize the amount of any surface film). The inset indicates schematically the shape of the section analyzed and the locations analyzed using EDXS.

Although the TEM image itself is not clear in terms of showing direct evidence of the IL generated film, the EDXS spectra (Fig. 9) at the four points indicated clearly show that the surface is of a different composition to the bulk. In particular, the appearance of P and S and a greater concentration of C and O is consistent with the presence of both cation and anion within this surface film, as indicated by the other characterization techniques discussed above. A good indication of the thickness of the film can be estimated here from the point at which the additional elements are no longer detected. The distance from B to D is  $\sim 150$  nm and this would appear to represent the thickness of the IL surface film generated in a 65 h period. Given that prior work<sup>23,29</sup> has suggested that a longer im-

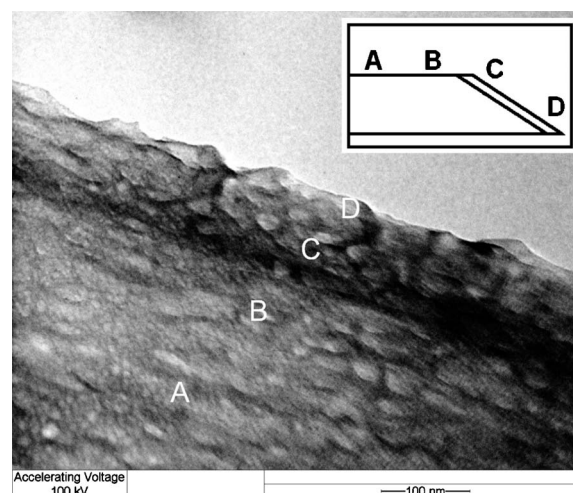


**Figure 8.** Sectioned TEM image of a  $[\text{P}_{66614}][\text{NTf}_2]$  treated AZ31 alloy surface. In this case, the specimen was immersed for 65 h to develop a thicker surface film. The specimen was microtomed to  $\sim 40$  nm thickness at its thickest point (roughly A and B), tapering to a triangular edge at point D. Points A and B are of a flat, bulk Mg alloy surface (uncoated), whereas points C and D represent the IL-coated AZ31. Image acquired using an accelerating voltage of 100 kV and magnification of  $\sim 200,000\times$ . Inset is side-view schematic representing point designation for EDXS capture.

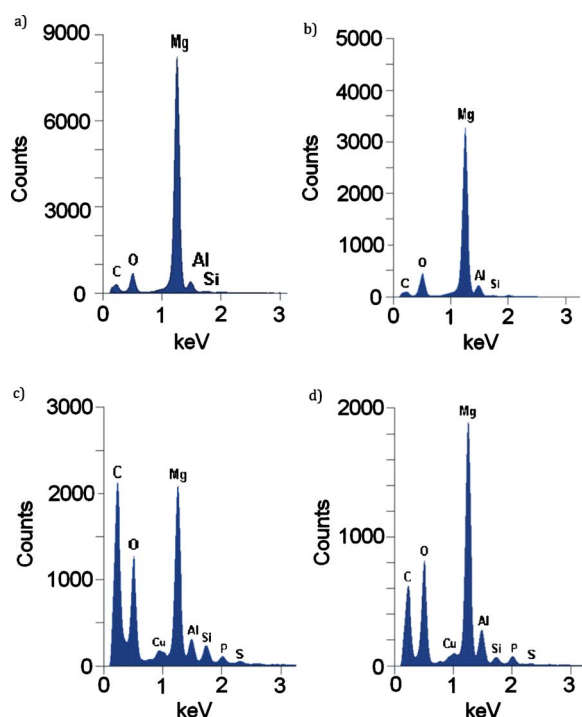


**Figure 9.** (Color online) EDXS elemental analysis of the microtomed TEM specimen shown in Fig. 8; points of analysis are as shown in the inset. Spectra are displayed for 0–3 keV from points A to D. Accelerating voltage of 100 kV used and 25 nm spot size for each of the point elemental analyses with a magnification of  $\sim 200,000\times$ .

mersion period leads to a thicker, less protective (in terms of corrosion) film, the 20 h film would be expected to be less than 100 nm thick.

### Conclusion

We have confirmed the presence of an  $\sim 100$  nm thick film on the surface of the AZ31 magnesium alloy when it is exposed to the IL trihexyl(tetradecyl)phosphonium bis(trifluoromethanesulfonyl)amide for  $> 20$  h. The use of complementary techniques, featuring varying degrees of surface sensitivity, from monolayer to bulk film analysis, provided improved insight into the nature and morphology of the film than what could not have been obtained otherwise. Grazing angle XRD showed that the film was amorphous and the chemical analysis of the surface using XPS and TOF-SIMS indicated that the surface was a complex multilayered structure, containing entrapped (or residual) intact cation and anion on the topmost surface followed by breakdown products, most likely to be anion breakdown products such as metal fluorides or smaller residues of the  $[\text{NTf}_2]^-$  anion. This is consistent with the observations of surface film formation on a reactive lithium metal anode exposed to a pyrrolidinium  $[\text{NTf}_2]^-$  IL.<sup>37</sup> The solid-state  $^{19}\text{F}$  NMR confirmed that there were several fluorine containing compounds present within the surface film and the electron microscopy, in particular the TEM/EDXS of a microtomed section, indicated that the film thickness was likely to be of the order of 100 nm. Based on our understanding of the solid electrolyte interphase layer formation on lithium metal<sup>37</sup> and on the observation that this particular IL appears to improve the corrosion properties of the AZ31 alloy,<sup>23,29,36</sup> we would conclude that this thin surface film forms primarily as a result of the breakdown of the  $[\text{NTf}_2]^-$  anion, which have been well documented and discussed previously by us<sup>38</sup> and others.<sup>39</sup> Finally, the general nature of the film appears to consist of an outer, IL and IL-product (in particular metal fluoride) dominated layers composed of breakdown products of the  $[\text{NTf}_2]^-$  anion and the entrained/precipitated  $[\text{P}_{66614}]^+$  cation. This film coexists with magnesium oxide/hydroxide species, which

are either present initially or formed during treatment. In light of these findings, the observed corrosion protection provided by this treatment<sup>7,28,29</sup> is not surprising; metal fluoride salts are insoluble and stable and the presence of the hydrophobic alkyl chain (in  $[\text{P}_{66614}]^+$ ) provides an additional barrier. These insights help to inform future research in this area, providing direction for IL design for protective coatings.

### Acknowledgments

We are grateful to Colin Veitch (CSIRO Materials Science and Engineering), Selwyn Glanville (Monash University MCEM), and Nicki Agron-Olshina (CSIRO Minerals) for their assistance in the TEM and XRD measurements. In addition, we acknowledge Franck Fougeron [Ecole Catholique d'Arts et Métiers (ECAM) internship] for his assistance in the acquisition of the NMR data. We also acknowledge the Australian Research Council for the financial support through DP0986205 and LE0560975.

Deakin University assisted in meeting the publication costs of this article.

### References

1. I. J. Polmear, *Light Alloys: Metallurgy of the Light Metals*, pp. 240–242, John Wiley & Sons, New York (1995).
2. Q. Miao, L. X. Hu, E. D. Wang, S. J. Liang, and H. Y. Chao, *Int. J. Mod. Phys. B*, **23**, 984 (2009).
3. G. L. Song and A. Atrens, *Adv. Eng. Mater.*, **1**, 11 (1999).
4. L. Commin, M. Dumont, J. E. Masse, and L. Barrallier, *Acta Mater.*, **57**, 326 (2009).
5. F. Yang, S. M. Yin, S. X. Li, and Z. F. Zhang, *Mater. Sci. Eng., A*, **491**, 131 (2008).
6. W. K. Hamblin, *The Earth's Dynamic Systems: A Textbook in Physical Geology*, p. 72, Macmillan, New York (1989).
7. N. Birbilis, P. C. Howlett, D. R. MacFarlane, and M. Forsyth, *Surf. Coat. Technol.*, **201**, 4496 (2007).
8. N. Winzer, A. Atrens, W. Dietzel, G. Song, and K. U. Kainer, *JOM*, **59**, 49 (2007).
9. S. Felio, A. Pardo, M. C. Merino, A. E. Coy, F. Viejo, and R. Arrabal, *Appl. Surf. Sci.*, **255**, 4102 (2009).
10. J. E. Gray and B. Luan, *J. Alloys Compd.*, **336**, 88 (2002).
11. F. Stippich, E. Vera, G. K. Wolf, G. Berg, and C. Friedrich, *Surf. Coat. Technol.*, **103–104**, 29 (1998).
12. G. S. Wu, K. J. Ding, X. Q. Zeng, X. M. Wang, and S. S. Yao, *Scr. Mater.*, **61**, 269 (2009).
13. C. J. Chen, M. C. Wang, D. S. Wang, R. Jin, and Y. M. Liu, *J. Alloys Compd.*, **438**, 321 (2007).
14. X. Yu, J. Wang, M. L. Zhang, P. P. Yang, L. H. Yang, D. X. Cao, and J. Q. Li, *Solid State Sci.*, **11**, 376 (2009).
15. G. Yan, G. Wang, G. Dong, G. Fan, L. Zhang, and M. Zhang, *J. Alloys Compd.*, **463**, 458 (2008).
16. Y. L. Cheng, H. L. Wu, Z. H. Chen, H. M. Wang, Z. Zhang, and Y. W. Wu, *Trans. Nonferrous Met. Soc. China*, **17**, 502 (2007).
17. X. M. Wang, X. Q. Zeng, G. S. Wu, S. S. Yao, and Y. J. Lai, *J. Alloys Compd.*, **437**, 87 (2007).
18. M. F. Montemor, A. M. Simoes, and M. J. Carmezim, *Appl. Surf. Sci.*, **253**, 6922 (2007).
19. J. H. Hu, S. K. Guan, C. L. Zhang, C. X. Ren, C. L. Wen, Z. Q. Zeng, and L. Peng, *Surf. Coat. Technol.*, **203**, 2017 (2009).
20. T. Ishizaki, I. Shigematsu, and N. Saito, *Surf. Coat. Technol.*, **203**, 2288 (2009).
21. L. P. Xu, F. Pan, G. N. Yu, L. Yang, E. L. Zhang, and K. Yang, *Biomaterials*, **30**, 1512 (2009).
22. F. Witte, N. Hort, C. Vogt, S. Cohen, K. U. Kainer, R. Willumeit, and F. Feyerabend, *Curr. Opin. Solid State Mater. Sci.*, **12**, 63 (2008).
23. M. Forsyth, W. C. Neil, P. C. Howlett, D. R. MacFarlane, B. R. W. Hinton, N. Rocher, T. F. Kemp, and M. E. Smith, *ACS Appl. Mater. Inter.*, **1**, 1045 (2009).
24. W. C. Neil, M. Forsyth, P. C. Howlett, C. R. Hutchinson, and B. R. W. Hinton, *Corros. Sci.*, **51**, 387 (2009).
25. P. C. Howlett, T. Khoo, G. Mooketsi, J. Efthimiadis, D. R. MacFarlane, and M. Forsyth, *Electrochim. Acta*, **55**, 2377 (2010).
26. P. C. Howlett, W. Neil, T. Khoo, J. Sun, M. Forsyth, and D. R. MacFarlane, *Isr. J. Chem.*, **48**, 313 (2008).
27. P. C. Howlett, S. Zhang, D. R. MacFarlane, and M. Forsyth, *Aust. J. Chem.*, **60**, 43 (2007).
28. P. C. Howlett, S. K. Tan, S. Zhang, J. Efthimiadis, D. R. MacFarlane, and M. Forsyth, Paper 79 presented at Corrosion and Prevention 2006, ACA (Australian Corrosion Association), Hobart, Tasmania (2006).
29. M. Forsyth, P. C. Howlett, S. K. Tan, D. R. MacFarlane, and N. Birbilis, *Electrochem. Solid-State Lett.*, **9**, B52 (2006).
30. W. Simka, D. Puszczczyk, and G. Nawrat, *Electrochim. Acta*, **54**, 5307 (2009).
31. J. M. Pringle, D. R. MacFarlane, and M. Forsyth, *Synth. Met.*, **155**, 684 (2005).
32. K. R. Seddon, *J. Chem. Technol. Biotechnol.*, **68**, 351 (1997).
33. K. J. Fraser and D. R. MacFarlane, *Aust. J. Chem.*, **62**, 309 (2009).

34. J. Sun, P. C. Howlett, D. R. MacFarlane, J. Lin, and M. Forsyth, *Electrochim. Acta*, **54**, 254 (2008).
35. D. R. MacFarlane, M. Forsyth, P. C. Howlett, J. M. Pringle, J. Sun, G. Annat, W. Neil, and E. I. Izgorodina, *Acc. Chem. Res.*, **40**, 1165 (2007).
36. D. R. MacFarlane, J. M. Pringle, P. C. Howlett, and M. Forsyth, *Phys. Chem. Chem. Phys.*, **12**, 1659 (2010).
37. P. C. Howlett, N. Brack, A. F. Hollenkamp, M. Forsyth, and D. R. MacFarlane, *J. Electrochem. Soc.*, **153**, A595 (2006).
38. P. C. Howlett, E. I. Izgorodina, M. Forsyth, and D. R. MacFarlane, *Z. Phys. Chem.*, **220**, 1483 (2006).
39. N. Amir, Y. Vestfrid, O. Chusid, Y. Gofer, and D. Aurbach, *J. Power Sources*, **174**, 1234 (2007).